Understanding thickness-dependent stability of tungsten-doped indium oxide transistors ⊘

Hyunjin Kim ⓘ ; Hyun-Sik Choi ⓘ ; Gyungwon Yun ⓘ ; Won-Ju Cho ✉ ⓘ ; Hamin Park ✉ ⓘ

Check for updates

View Online

Export Citation

Articles You May Be Interested In

Single β-Ga$_2$O$_3$ nanowire based lateral FinFET on Si

Appl. Phys. Lett. (April 2022)

Surface and core contribution to 1/f-noise in InAs nanowire metal-oxide-semiconductor field-effect transistors

Appl. Phys. Lett. (July 2013)

Low-frequency 1/f noise in MoS$_2$ transistors: Relative contributions of the channel and contacts

Appl. Phys. Lett. (April 2014)

Understanding thickness-dependent stability of tungsten-doped indium oxide transistors

Hyunjin Kim,[1] (iD) Hyun-Sik Choi,[2] (iD) Gyungwon Yun,[1] (iD) Won-Ju Cho,[2,a] (iD) and Hamin Park[1,a] (iD)

AFFILIATIONS

[1]Department of Electronic Engineering, Kwangwoon University, 20, Gwangun-ro, Nowon-gu, Seoul 01897, Republic of Korea
[2]Department of Electronic Materials Engineering, Kwangwoon University, 20, Gwangun-ro, Nowon-gu, Seoul 01897, Republic of Korea

[a]Authors to whom correspondence should be addressed: chowj@kw.ac.kr and parkhamin@kw.ac.kr

ABSTRACT

In this study, the influence of the thickness of the channel layer on the electrical properties and stability of tungsten-doped indium oxide (IWO) thin-film transistors (TFTs) was investigated. Although oxide-semiconductor TFTs, particularly indium gallium zinc oxide, are promising, problems related to oxygen vacancies have led to their instability. In contrast, IWO has proven to be a compelling alternative because of its robust resistance to oxygen vacancies. IWO TFTs with varying channel thicknesses (10, 20, and 30 nm) were fabricated, and the device parameters, such as threshold voltage (V_{th}), subthreshold swing (SS), field-effect mobility (μ_{FE}), and on/off current ratio (I_{on}/I_{off}), were analyzed. It was found that as the channel thickness increased, V_{th} exhibited a negative shift and SS increased, indicating an increase in carrier concentration. This phenomenon is attributed to the bulk trap density, in particular to oxygen vacancies. Negative bias stress tests confirmed the influence of the oxygen vacancies, with thicker channels showing more pronounced shifts. Low-frequency noise measurements were consistent with the carrier number fluctuation model, indicating that defects within the channel region contribute to the observed noise. The study concludes that identifying an optimal channel thickness during device manufacturing is crucial for improved TFT performance, with 20 nm devices characterized by high μ_{FE} and comparable trap density to 10 nm. This study provides valuable insight into the nuanced relationship between the channel thickness, trap density, and electrical performance of IWO TFTs.

Recently, the development of high-performance and energy-efficient electronic devices has driven the exploration of novel materials and device architectures. Oxide-semiconductor thin-film transistors (TFTs) have emerged as promising candidates for next-generation electronic applications.[1] The electron transport path in oxide semiconductors is formed by the overlapping of the s orbitals of metal ions, allowing high mobility to be achieved. The increasing fascination with oxide semiconductors arises from their distinctive electrical, optical, and structural characteristics, which present novel opportunities for the development of advanced transistor technologies.[2–4] Transistors constructed from silicon have historically formed the foundation of contemporary electronic devices. However, as the demand for higher performance and flexible electronics increases, alternative materials have become essential. Oxide semiconductors offer a compelling alternative to conventional silicon for thin-film transistor applications owing to their intrinsic transparency, wide bandgap, and exceptional electron mobility.[5–7] Amorphous silicon suffers from low electron mobility, limiting its application in high-speed electronics.[8,9] While polycrystalline silicon achieves higher electron mobility than amorphous silicon, it requires excimer laser annealing to reach its optimal electrical performance.[10,11] In contrast, oxide semiconductors can be processed at relatively low temperatures, enabling their integration into various applications without compromising electrical performance. A notable example of this class of materials is indium gallium zinc oxide (IGZO), which has gained prominence owing to its exceptional electrical properties, including high carrier mobility and low off-state leakage current.[1,12,13]

Despite the promising attributes of oxide-semiconductor TFTs, there are still challenges and gaps in our understanding. One critical problem arises from the weak bond dissociation energy between gallium (Ga) and oxygen, which makes the suppression of oxygen vacancies difficult.[14,15] This challenge is a major contributor to the instability of IGZO TFTs, and the susceptibility of IGZO to oxygen vacancies affects the long-term stability and electrical performance of these devices. In contrast, our focus was on tungsten-doped indium oxide (IWO), a less explored oxide semiconductor. Tungsten exhibits a

strong bond dissociation energy with oxygen, suggesting robust resistance to oxygen vacancies.[16–18] This unique property makes IWO a compelling alternative that offers not only high carrier mobility but also improved stability, thus addressing the critical challenge faced by IGZO. Therefore, recent studies on IWO TFTs have begun to demonstrate outstanding device performance.[19–22] However, there is a lack of research on the electrical properties and mechanisms that depend on material parameters, such as the thickness of the IWO.

In this study, IWO TFTs were fabricated and their electrical properties for channel thicknesses (T_{ch}) of 10, 20, and 30 nm were characterized. The analysis encompassed crucial device parameters such as threshold voltage (V_{th}), subthreshold swing (SS), field-effect mobility (μ_{FE}), and on/off current ratio (I_{on}/I_{off}). With an increase in T_{ch}, V_{th} was negatively shifted and SS increased. The SS values enabled the determination of the total trap density (N_t). Furthermore, an investigation of the electrical stability under negative bias stress (NBS) revealed consistent negative shifts across all TFTs, with a more pronounced effect observed in the TFT with a thicker T_{ch}. It is worth mentioning that the shared gate oxide material of SiO_2 of the TFTs emphasizes that the differences in trap density and the degree of negative shift are attributed to the bulk trap density (N_{bk}), notably oxygen vacancies. Finally, the low-frequency noise (LFN) was estimated to quantify the border trap density (N_{bt}). This revealed a higher power spectral density for TFTs with a thicker T_{ch}, indicating a higher trap density beyond the interface region.

The cross-sectional structure of a bottom-gated IWO TFT is shown in Fig. 1(a). A highly doped p-type Si wafer with a low resistance of less than 0.005 Ω·cm served as the gate electrode. A 90 nm thick SiO_2 layer was thermally grown on top of the wafer as the gate oxide layer. The channel layer was formed by depositing a 10/20/30 nm IWO film by RF sputtering from a source composed of In_2O_3 and WO_3 with a ratio of 99:1 by weight. A positive photoresist (PR) was then applied to the film and the channel layer was patterned with a 30:1 buffered oxide etchant (BOE). Following the channel layer patterning, 150 nm thick titanium was deposited for the source/drain electrodes using an e-beam evaporator. The device was annealed at 300 °C to improve interface properties and adjust the amount of oxygen vacancies. No additional layer was deposited on top of the IWO channel. The dimensions of the channel layer, denoted as width (W) and length (L), were set to 20 and 12 μm, respectively. X-ray photoelectron spectroscopy (XPS) spectra were obtained using a Thermo Fisher Scientific XPS system. Current–voltage (I–V) characteristic curves were obtained in a dark ambient environment using a Keithley 2614B source meter. In addition, LFN measurements were performed using a 35760A dynamic signal analyzer with an SR570 low-noise current amplifier. Throughout the experiments, all devices were fully grounded. The detailed characteristics, including transmission electron microscope (TEM) images (Fig. S1), x-ray Diffraction (XRD) spectra (Fig. S2), depth-profiled XPS spectra (Fig. S3), atomic force microscope (AFM) profiles (Fig. S4), and optical microscope images (Fig. S5), are provided in the supplementary material.

The binding energy of the IWO channel was analyzed by examining the O 1s (black), In 3d (red), and W 4f (blue) XPS spectra, as shown in Fig. 1(b). The O 1s spectrum showed two components at binding energies of 530 eV, corresponding to the binding energies of O^{2-} surrounded by In atoms, and 532 eV, corresponding to both oxygen vacancies and adsorbed oxygen.[23] The relatively low intensity of the 532 eV peak indicates that the oxygen vacancies were restrained
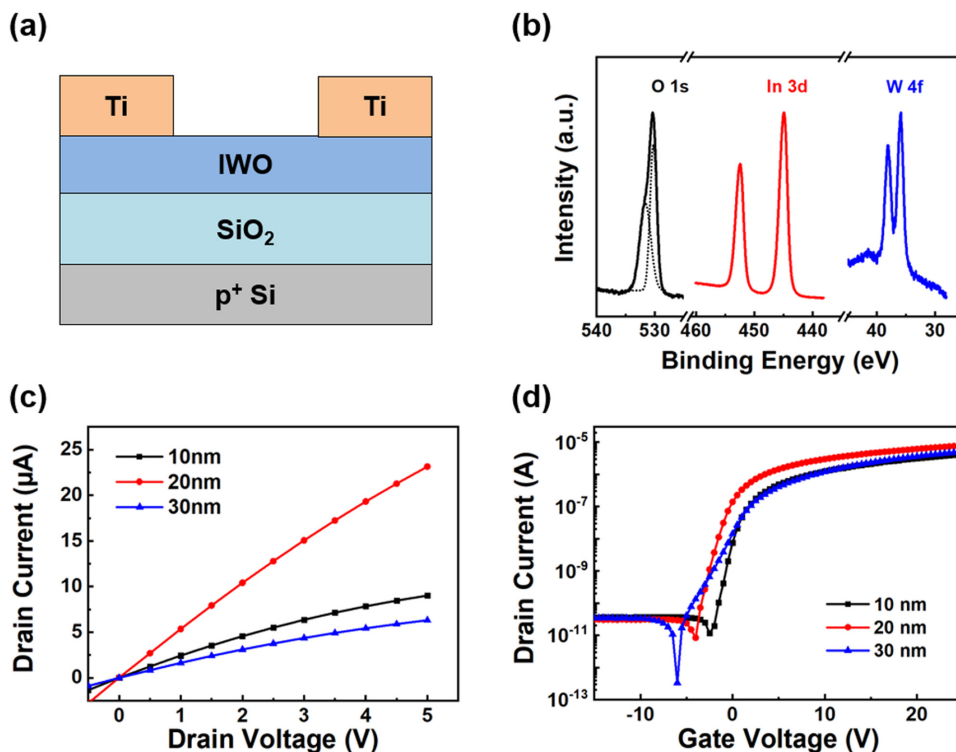

FIG. 1. (a) Cross-sectional structure of the IWO TFT and (b) x-ray photoelectron spectroscopy spectra (XPS) of O 1s (black), In 3d (red), and W 4f (blue). (c) Output and (d) transfer characteristics of the IWO TFT.

TABLE I. Extracted electrical parameters of the IWO TFTs with different channel thicknesses.

	V_{on} (V)	V_{th} (V)	μ_{FE} (cm^{2}V^{-1}s^{-1})	SS (V/dec)	I_{on}/I_{off}	N_t (cm^{-2}eV^{-1})
10 nm	−2	−0.6	8.1	0.85	∼10^6	3.32×10^{12}
20 nm	−4	−1.3	11.8	1	∼10^6	3.96×10^{12}
30 nm	−6	−0.2	10	1.74	∼10^6	7.03×10^{12}

during the process.[24] The In 3d spectrum showed a doublet with binding energies of 445 eV for In $3d_{5/2}$ and 452 eV for In $3d_{3/2}$, which correspond to the binding energies of the In^{3+} ion in the In$_2$O$_3$ lattice, indicating the oxidation of In atoms to In^{3+} ions in the lattice.[25] The W 4f spectrum at 38 eV for W $4f_{5/2}$ and 36 eV for W $4f_{7/2}$ indicates that most tungsten atoms are oxidized to +6 valence and exist in the In$_2$O$_3$ lattice.[26,27]

The electrical characteristics of the IWO TFTs are shown in Figs. 1(c) and 1(d). Figure 1(c) presents the output characteristics measured at gate–source voltage (V_{GS}) = 5 V. The detailed output characteristics are provided in the supplementary material (Fig. S6). It is noticeable that the drain current increases at the transition of T_{ch} from 10 to 20 nm. However, a decrease in drain current was observed at the transition of T_{ch} from 20 to 30 nm. This trend indicates that a thicker channel accommodates more electrons in the channel region; however, a paradoxical decrease in current is observed for the 30 nm channel TFT. To elucidate this instability, the transfer characteristic curves were measured under the linear region at V_{DS} = 0.5 V, as shown in Fig. 1(d). The main electrical parameters, including on voltage (V_{on}), V_{th}, SS, μ_{FE}, and I_{on}/I_{off}, were extracted as listed in Table I. Negligible hysteresis was observed between the forward and reverse sweeps in the dual-sweep transfer curves in the supplementary material (Fig. S7). V_{on}, the point at which the drain current transitions from the off-region, shifts toward the negative direction with increasing T_{ch}, indicating an increase in the carrier concentration. Simultaneously, the SS exhibited a linear increase in T_{ch}. However, μ_{FE} showed a slight decrease when T_{ch} reached 30 nm. This decrease can be attributed to the total trap density (N_t) near the interface between the channel and the gate oxide layer. To elucidate the origin of the different trap densities, we measured AFM profiles (supplementary material, Fig. S4). The root mean square (RMS) values for the surface roughness were 0.134, 0.199, and 0.258 nm for the 10, 20, and 30 nm IWO films, respectively, revealing a more uneven surface with thicker channels.

The extracted SS values are closely correlated with the total trap density, as the following equation shows:[28,29]

$$N_t = N_{it} + N_{bk} = \left(\frac{SS * \log(e)}{kT/q} - 1 \right) \frac{C_{ox}}{q},$$

where N_{it} is the interface trap density, N_{bk} is the bulk trap density, T is the absolute temperature, k is the Boltzmann constant, q is the electronic charge, and C_{ox} is the capacitance of the gate oxide per unit area. Given the consistent deposition conditions for IWO films, where the only variables are the deposition time and the uniformity of the gate oxide material (SiO$_2$) across all TFTs, devices with similar interfaces near the gate oxide will have similar N_{it} values. Consequently, the effect of trap density attributable to N_{it} can be disregarded. The degradation in the SS values is predominantly dependent on the N_{bk} values, which emphasizes the role of the bulk trap density as T_{ch} increases.[28,29]

As a result, the defect states accountable for the degradation of the SS value in the channel layer were the primary focus. This rationale prompted us to examine four different types of defects: donor- and acceptor-like states that exist at both the shallow and deep levels. Typically, deep-level donor-like states reside beneath the Fermi level so that they have no influence on the transfer characteristic owing to the neutralization effect—filled by electrons, resulting in neutralized donor-like states. The exclusion of acceptor-like states at both the shallow and deep levels follows this evolution, as these defects trigger a different V_{th} shift mechanism, leading to a positive shift in V_{th}. Consequently, the critical role of the SS value degradation is attributed to donor-like states at the shallow level.[29]

Among the different types of donor-like states that affect transfer characteristic, oxygen vacancies take precedence.[30,31] Normally, these oxygen vacancies are located in the channel region, and form a neutral state when they reside beneath the Fermi level, acting as deep donor-like states. However, when these defects migrate toward the Fermi level, they undergo a ionization, releasing free electrons to the channel region and adopting a positively charged state (Vo → Vo$^+$ + e$^-$, Vo → Vo^{2+} + 2e$^-$).[32] Consequently, with an increase in T_{ch}, there is a corresponding increase in the number of defects within the channel, augmenting the electron population in this region. This influx manifests itself in a negative shift in the transfer characteristic curve and a concurrent deterioration in the SS value.

To elucidate the effect of the oxygen vacancies, a comprehensive NBS test was performed. Bias stability is a crucial aspect for the practical application of electronic devices and can reveal the degradation mechanism of channel materials and interfaces. To assess bias stability,
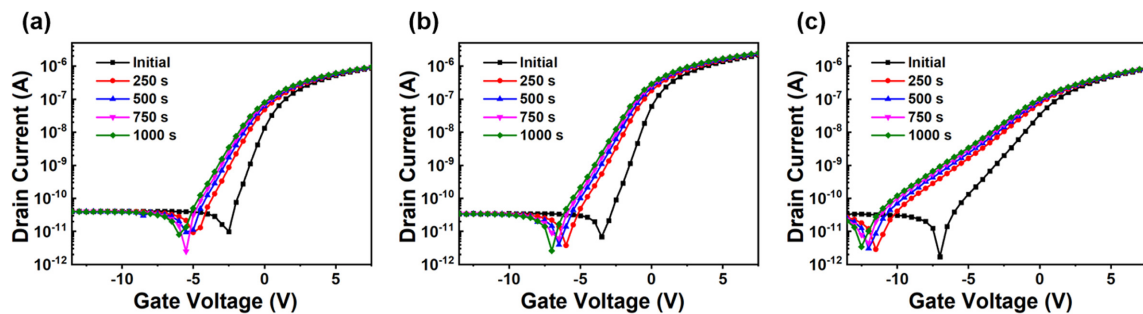
FIG. 2. Transfer characteristic curves under the NBS (V_{GS} = −15 V) of the IWO TFTs with (a) 10, (b) 20, and (c) 30 nm thickness.
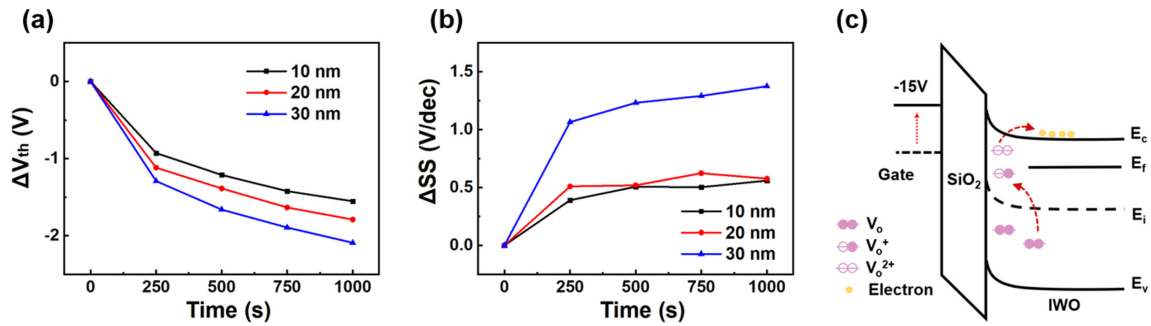
FIG. 3. Time-dependent evolution of (a) threshold voltage and (b) subthreshold swing with different channel thicknesses. (c) Energy band diagram describing oxygen vacancies under negative bias stress ($V_{GS} = -15$ V, $V_{DS} = 0$ V).

a bias stress test was performed to demonstrate the bias stability of the IWO TFTs. To demonstrate the NBS-induced instability, a V_{GS} of -15 V with a grounded drain was applied and the transfer characteristics were measured after 250 s for a cumulative duration of 1000 s in a dark ambient environment. Figures 2(a)–2(c) show the transfer characteristics under NBS of the IWO TFTs with different T_{ch} of 10, 20, and 30 nm. A consistent observation across all TFTs was a V_{th} shift in the negative direction, although the altered values of the electrical parameters varied somewhat, as illustrated in Fig. 3. Figures 3(a) and

3(b) show the time-dependent changes of V_{th} and SS, respectively, under NBS. It is noteworthy that the changes of V_{th} and SS increase with increasing T_{ch}, even under identical stress conditions. This increase was attributed to the presence of oxygen vacancies in the channel region.

As previously stated, the location of oxygen vacancies in relation to the Fermi level determines whether they exist in positive or neutral states. Under normal conditions, the majority of oxygen vacancies remained in a neutral state. However, when subjected to NBS, the
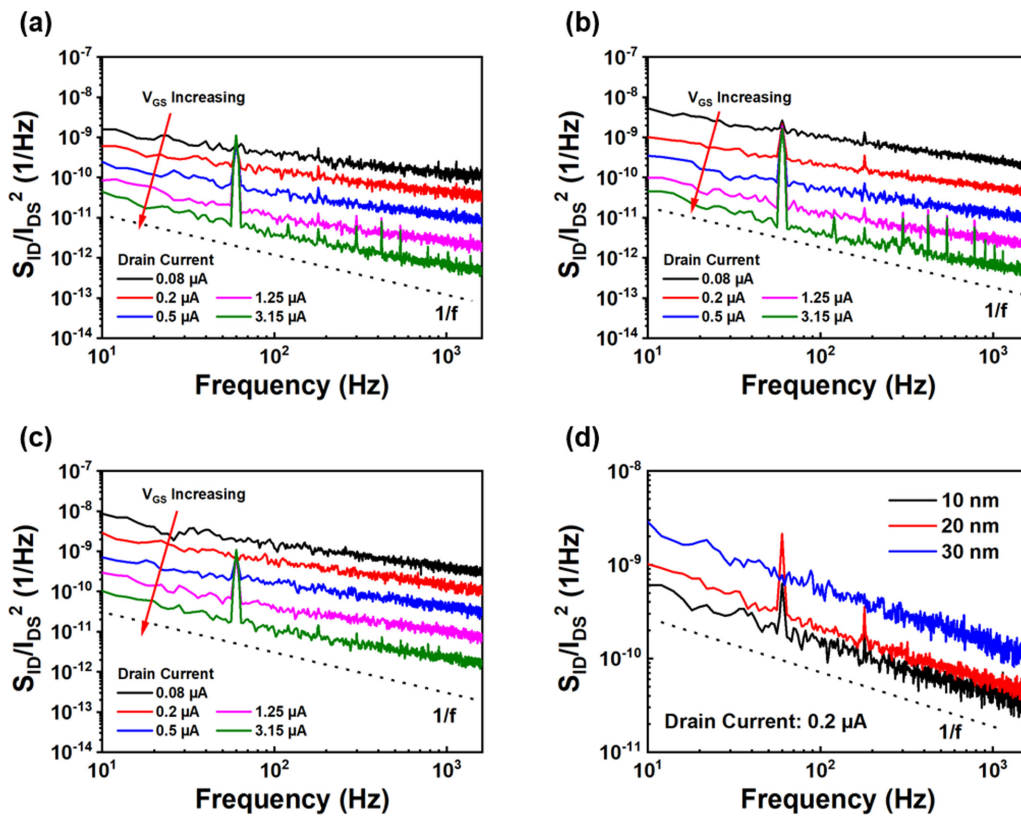
FIG. 4. Normalized power spectral density for IWO TFTs with varying channel thicknesses: (a) 10, (b) 20, and (c) 30 nm. (d) Comparative analysis of low-frequency noise (LFN) for different channel thicknesses when the drain current is fixed at 0.2 μA.

energy band near the interface underwent an upward curvature, so that the neutral oxygen vacancies may be located above the Fermi level, as shown in Fig. 3(c). As a result, the oxygen vacancies located above the Fermi level ionized into positively charged ions.[32–34] Analysis of the SS values presented in Table I reveals that the quantity of oxygen vacancies in the channel region varies as a function of T_{ch}. Consequently, the quantity of oxygen vacancies ionizing to V_O^+/V_O^{2+} is different even when the same NBS is applied, leading to different changes in the electrical parameters. At a T_{ch} of 10 nm, which is characterized by a smaller quantity of oxygen vacancies, the change is minimal, escalating with T_{ch} and reaching its zenith at 30 nm. Consequently, the 30 nm TFT has the highest concentration of V_O^+/V_O^{2+} and, accordingly, the most pronounced alterations in V_{th} and SS.

To fully understand the effects of defects in the IWO channel layer, LFN measurements were performed. Figure 4 illustrates the normalized power spectral density (S_{ID}/I_{DS}^2) for three devices with different T_{ch}, measured in the linear region with V_{DS} maintained at 0.5 V. Here, S_{ID} represents the noise power spectral density and I_{DS} represents the drain current. The LFN measurements were performed by gradually increasing the drain current and sweeping the frequency range from 10 Hz to 1.61 kHz. The LFN results for the IWO TFTs at 10/20/30 nm are shown in Figs. 4(a)–4(c). In addition, Fig. 4(d) shows a comparative analysis of the power spectral density values at $I_{DS} = 0.2$ μA. All devices showed a decrease in the power spectral density with increasing I_{DS}, which correlates with the rise in V_{GS}, and uniformly followed a 1/f trend with a slope of −1. Furthermore,

Fig. 4(d) shows that the LFN level increased with increasing T_{ch} at the same current level.

To discern the predominant mechanism underlying the LFN in IWO TFTs with varying T_{ch}, an examination of the dependence of S_{ID}/I_{DS}^2 and $(g_m/I_{DS})^2$ on the drain current was performed for three distinct devices. Here, g_m represents the transconductance. In Figs. 5(a)–5(c), a log–log plot illustrates the variation of S_{ID}/I_{DS}^2 with respect to the drain current for IWO TFTs at a fixed frequency (20 Hz) with a T_{ch} of 10/20/30 nm. It is noticeable that the S_{ID}/I_{DS}^2 value exhibited a decreasing trend with increasing I_{DS}, which agrees well with the $(g_m/I_{DS})^2$ line. Prior research on LFNs in field-effect transistors (FETs) has employed three models to assess the LFN behavior. The carrier number fluctuation model (CNF, Δn) is influenced by the trap states within the interface or bulk of the channel region, and represents the noise generated by the repeated trapping and release of carriers in the channel.[35,36] In the case of oxide semiconductors, generation–recombination processes at bulk subgap traps, such as ionized oxygen vacancies mentioned above, in the channel also induce fluctuations in carrier number.[37–39] The carrier mobility fluctuation model (CMF, $\Delta\mu$) attributes the noise to bulk mobility fluctuations associated with phonon or impurity scattering in the channel region.[40,41] The third model, known as the correlated number mobility fluctuation model ($\Delta n-\Delta\mu$), assumes that the noise in the channel can arise from a combination of trap state and scattering effects, and provides a more comprehensive understanding.[42,43]

The predominant mechanism driving the LFN in FETs can be discerned by examining the dependence of S_{ID}/I_{DS}^2 on I_{DS} at a fixed
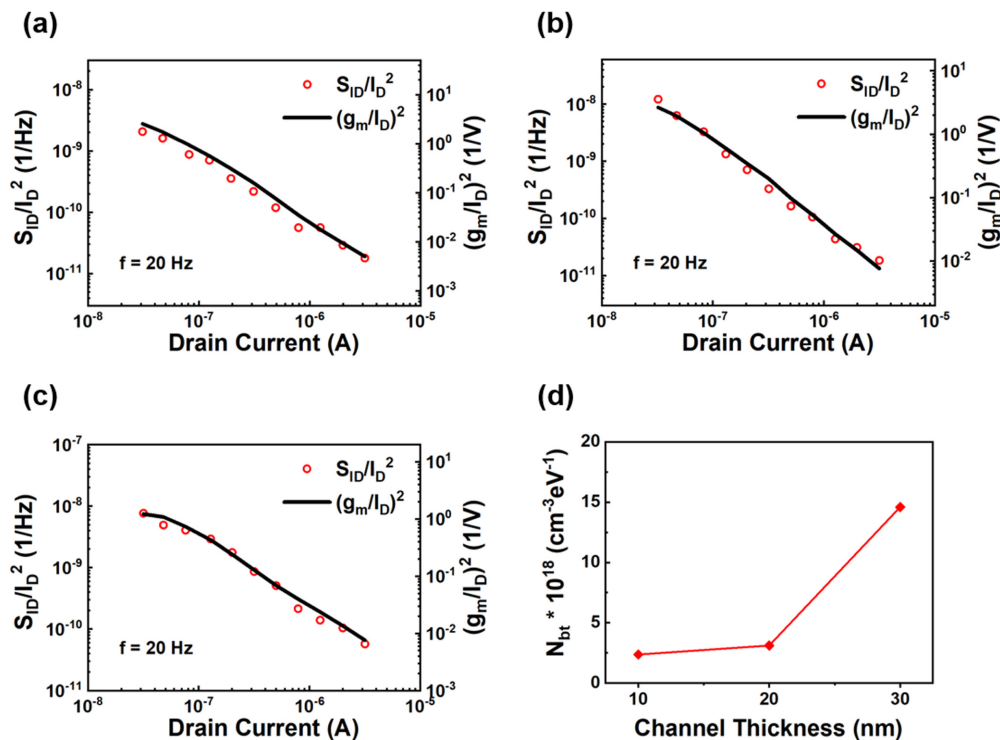

FIG. 5. Variation of S_{ID}/I_{DS}^2 (symbol) and $(g_m/I_{DS})^2$ (line) as a function of I_{DS} for IWO TFTs with varying channel thicknesses: (a) 10, (b) 20, and (c) 30 nm. (d) Border trap states as a function of the channel thickness.

frequency. According to the CNF model, S_{ID}/I_{DS}^2 is defined by the following equation:[36]

$$\frac{S_{ID}}{I_{DS}^2} = \frac{q^2 kT\lambda N_{bt}}{fWLC_{ox}^2}\left(\frac{g_m}{I_{DS}}\right)^2,$$

where λ represents the tunneling attenuation distance (approximately 0.1 nm in SiO_2), and N_{bt} signifies the border trap density. The strong correlation observed between S_{ID}/I_{DS}^2 and the $(g_m/I_{DS})^2$ line over a range of drain currents suggests that LFN can be attributed to the CNF model.[35,44,45] It is noteworthy that all devices, regardless of T_{ch}, conformed to the CNF model, as evidenced by the alignment of the LFN values with the $(g_m/I_{DS})^2$ line. Using the equation of the CNF model, the N_{bt} for each T_{ch} can be calculated, resulting in values of 2.37/3.12/$14.6 \times 10^{18}\,cm^{-3}\,eV^{-1}$, as shown in Fig. 5(d). As shown in Fig. 4(d), the increase in the power spectral density level is consistent with the augmented N_{bt} values as T_{ch} increases. This observation corroborates the previously analyzed correlation between T_{ch} and SS. An increase in T_{ch} led to an increase in both N_{bk} and N_{bt}, which contributed to a degradation in the SS value and the overall electrical performance.

In this study, the influence of IWO T_{ch} on the electrical properties and stability of fabricated TFTs was investigated. A negative shift in V_{th} and a continuous increase in SS were observed with increasing T_{ch}, which was attributed to a significant increase in N_{bk}. NBS induced a negative shift in the transfer curves to varying degrees as a function of T_{ch}, which can be attributed to the different amounts of positively charged oxygen vacancies. LFN measurements revealed a 1/f trend, with the noise power spectral density decreasing with increasing V_{GS}, and the density being higher for thicker channels at the same drain current, indicating the dominance of the carrier number fluctuation model. The N_{bt} values from the LFN conformed to the same thickness-dependence with the N_{bk} values from the SS analysis. A comparative analysis highlighted that 20 nm devices had the highest mobility and low trap density, emphasizing the importance of identifying an optimal T_{ch} during device manufacturing to improve performance. This comprehensive study, supported by the transfer characteristics, NBS, and LFN analyses, has significantly improved our understanding of the nuanced variations in trap density associated with different T_{ch} values in IWO TFTs, and provides valuable insights for device performance optimization. Future studies will aim to achieve a more extensive understanding of the stability of IWO TFTs, with a focus on considering additional device parameters to further optimize performance.

See the supplementary material for detailed material properties of IWO films and the electrical characteristics of IWO TFTs.

AUTHOR DECLARATIONS
Conflict of Interest

The authors have no conflicts to disclose.

Author Contributions

Hyunjin Kim and Hyun-Sik Choi contributed equally to this work.

Hyunjin Kim: Conceptualization (equal); Formal analysis (equal); Investigation (equal); Writing – original draft (equal). **Hyun-Sik Choi:** Conceptualization (equal); Investigation (equal); Methodology (equal); Resources (equal). **Gyungwon Yun:** Investigation (equal); Methodology (equal). **Won-Ju Cho:** Conceptualization (equal); Investigation (equal); Methodology (equal); Resources (equal); Supervision (equal). **Hamin Park:** Conceptualization (equal); Funding acquisition (equal); Investigation (equal); Supervision (equal); Writing – review & editing (equal).

DATA AVAILABILITY

The data that support the findings of this study are available from the corresponding authors upon reasonable request.

REFERENCES

[1] K. Nomura, H. Ohta, A. Takagi, T. Kamiya, M. Hirano, and H. Hosono, Nature **432**, 488 (2004).

[2] A. R. Choi, D. H. Lim, S. Y. Shin, H. J. Kang, D. Kim, J. Y. Kim, Y. Ahn, S. W. Ryu, and I. K. Oh, Chem. Mater. **36**(5), 2194 (2024).

[3] S. L. Gao, L. P. Qiu, J. Zhang, W. P. Han, S. Ramakrishna, and Y. Z. Long, Acs Appl. Electron. Mater. J. **6**(3), 1542 (2024).

[4] K. Nomura, T. Kamiya, H. Ohta, T. Uruga, M. Hirano, and H. Hosono, Phys Rev B **75**(3), 035212 (2007).

[5] H. Hosono, Thin Solid Films **515**(15), 6000 (2007).

[6] J. L. Shi, J. Y. Zhang, L. Yang, M. Qu, D. C. Qi, and K. H. L. Zhang, Adv. Mater. **33**(50), 2006230 (2021).

[7] T. Kim, C. H. Choi, J. S. Hur, D. Ha, B. J. Kuh, Y. Kim, M. H. Cho, S. Kim, and J. K. Jeong, Adv. Mater. **35**(43), 2204663 (2023).

[8] F. Morin, Microelectron. Eng. **19**(1–4), 171 (1992).

[9] G. W. Shim, W. Hong, J. H. Cha, J. H. Park, K. J. Lee, and S. Y. Choi, Adv. Mater. **32**(35), 1907166 (2020).

[10] M. Mitani, T. Endo, S. Tsuboi, T. Okada, G. Kawachi, and M. Matsumura, Jpn. J. Appl. Phys., Part 1 **49**(12), 124001 (2010).

[11] T. Goto, K. Saito, F. Imaizumi, M. Hatanaka, M. Takimoto, M. Mizumura, J. Gotoh, H. Ikenoue, and S. Sugawa, IEEE Trans. Electron Devices **65**(8), 3250 (2018).

[12] J. Zhang, Z. H. Lin, Z. C. Zhang, K. Xu, H. Y. Dou, B. Yang, A. Charnas, D. Q. Zheng, X. H. Zhang, H. Y. Wang, and P. D. Ye, IEEE Trans. Electron Devices **70**(12), 6651 (2023).

[13] S. Sallis, K. T. Butler, N. F. Quackenbush, D. S. Williams, M. Junda, D. A. Fischer, J. C. Woicik, N. J. Podraza, B. E. White, A. Walsh, and L. F. J. Piper, Appl. Phys. Lett. **104**(23), 232108 (2014).

[14] H. L. Li, M. Y. Qu, and Q. Zhang, IEEE Electron Device Lett. **34**(10), 1268 (2013).

[15] J. A. Dean, *Lange's Handbook of Chemistry* (McGraw-Hill, New York, N.Y, 1999).

[16] N. Tiwari, M. Rajput, R. A. John, M. R. Kulkarni, A. C. Nguyen, and N. Mathews, ACS Appl. Mater. Interfaces **10**(36), 30506 (2018).

[17] M. G. Kim, H. S. Kim, Y. G. Ha, J. Q. He, M. G. Kanatzidis, A. Facchetti, and T. J. Marks, J. Am. Chem. Soc. **132**(30), 10352 (2010).

[18] A. Liu, G. X. Liu, H. H. Zhu, B. Shin, E. Fortunato, R. Martins, and F. K. Shan, J. Mater. Chem. C **4**(20), 4478 (2016).

[19] D. B. Ruan, P. T. Liu, K. J. Gan, Y. C. Chiu, C. C. Hsu, and S. M. Sze, Appl. Phys. Lett. **116**(18), 182104 (2020).

[20] B. Grisafe, W. Chakraborty, H. Ye, I. Lightcap, K. Ni, and S. Datta, in IEEE Symposium on VLSI Technology, 2020.

[21] Z. H. Li, T. C. Chiang, P. Y. Kuo, C. H. Tu, Y. Kuo, and P. T. Liu, Adv. Sci. **10**(9), 2205481 (2023).

[22] G. Choe, J. Kwak, and S. M. Yu, IEEE Trans. Electron Devices **71**(1), 231 (2024).

[23]T. Tohsophon, A. Dabirian, S. De Wolf, M. Morales-Masis, and C. Ballif, APL Mater. **3**(11), 116105 (2015).

[24]J. G. Kim, J. E. Lee, S. M. Jo, B. D. Chin, J. Y. Baek, K. J. Ahn, S. J. Kang, and H. K. Kim, Sci. Rep. **8**, 12019 (2018).

[25]M. Yang, J. H. Feng, G. F. Li, and Q. Zhang, J. Cryst. Growth **310**(15), 3474 (2008).

[26]X. F. Li, Q. Zhang, W. N. Miao, L. Huang, Z. J. Zhang, and Z. Y. Hua, J. Vac. Sci. Technol. A **24**(5), 1866 (2006).

[27]T. Gan, J. M. Li, L. L. Wu, J. Q. Zhang, X. Hao, Q. Y. Zhang, R. X. Li, and W. H. Shi, Mater. Sci. Semicond. Process **138**, 106257 (2022).

[28]X. W. Ding, J. H. Zhang, J. Li, H. Zhang, W. M. Shi, X. Y. Jiang, and Z. L. Zhang, Superlattices Microstruct. **63**, 70 (2013).

[29]B. H. Lee and S. Y. Lee, Phys. Status Solidi A **215**(12), 1700698 (2018).

[30]B. Murugan and S. Y. Lee, Solid-State Electron. **200**, 108539 (2023).

[31]D. Lin, S. B. Pi, J. W. Yang, N. Tiwari, J. H. Ren, Q. Zhang, P. T. Liu, and H. P. Shieh, Semicond. Sci. Technol. **33**(6), 065001 (2018).

[32]E. N. Cho, J. H. Kang, C. E. Kim, P. Moon, and I. Yun, IEEE Trans. Device Mater. Reliab. **11**(1), 112 (2011).

[33]C. D. Chen, C. N. Liu, J. W. Zheng, G. T. Li, S. Li, Q. Wu, J. Wu, and C. Liu, J. Inf. Disp. **20**(3), 161 (2019).

[34]G. T. Li, B. R. Yang, C. Liu, C. Y. Lee, Y. C. Wu, P. Y. Lu, S. Z. Deng, H. P. D. Shieh, and N. S. Xu, IEEE Electron Device Lett. **37**(5), 607 (2016).

[35]H. J. Kim, C. Y. Jeong, S. D. Bae, and H. I. Kwon, J. Vac. Sci. Technol. B **35**(1), 010601 (2017).

[36]A. L. McWhorter, *Semiconductor Surface Physics.* (University of Pennsylvania Press, Philadelphia, PA, 1957).

[37]S. Kim, Y. Jeon, J. H. Lee, B. D. Ahn, S. Y. Park, J. H. Park, J. H. Kim, J. Park, D. M. Kim, and D. H. Kim, IEEE Electron Device Lett. **31**(11), 1236 (2010).

[38]Y. H. Tai, C. Y. Chang, and C. L. Hsieh, J. Disp. Technol. **12**(7), 685 (2016).

[39]W. Shin, J. Y. Lee, R. H. Koo, J. Kim, J. H. Lee, S. Y. Lee, and S. T. Lee, Adv. Electron. Mater. **10**(2), 2300515 (2024).

[40]F. N. Hooge, IEEE Trans. Electron Devices **41**(11), 1926 (1994).

[41]H. S. Choi, S. Jeon, H. Kim, J. Shin, C. Kim, and U. I. Chung, Appl. Phys. Lett. **100**(17), 173501 (2012).

[42]P. K. Ko Kwok, K. Hung, C. Hu, and Y. C. Cheng, IEEE Trans. Electron Devices **37**(3), 654 (1990).

[43]O. R. G. Ghibaudo, C. Nguyen-Duc, F. Balestra, and J. Brin, Phys. Status Solidi A **124**, 571 (1991).

[44]G. B. Lee, C. K. Kim, M. S. Yoo, and Y. K. Choi, IEEE Trans. Electron Devices **67**(10), 4366 (2020).

[45]H. L. Ramírez, Y.-C. Chien, L. Hoffman, M. Nag, S. Haesler, S. Steudel, and J. Genoe, in Proceedings of the 25th International Conference on Noise and Fluctuations (ICNF), 2019, Vol. 1.

31 October 2024 07:24:50